In Situ Study of FePt Nanoparticles-Induced Morphology Development during Printing of Magnetic Hybrid Diblock Copolymer Films

Wei Cao, Shanshan Yin, Martin Bitsch, Suzhe Liang, Martina Plank, Matthias Opel, Manuel A. Scheel, Markus Gallei, Oliver Janka, Matthias Schwartzkopf, Stephan V. Roth, and Peter Müller-Buschbaum*

The development of magnetic hybrid films containing diblock copolymers (DBCs) and magnetic nanoparticles (NPs) by printing is a highly promising method for scalable and low-cost fabrication. During printing, the drying and arrangement kinetics of the DBC and magnetic NPs play an important role in the film formation concerning morphology and magnetic properties. In this study, the morphology evolution of ultrahigh molecular weight DBC polystyrene-block-poly(methyl methacrylate) and magnetic iron platinum (FePt) NPs is investigated with grazing-incidence small-angle X-ray scattering (GISAXS) in situ during printing. For comparison, a pure DBC film is printed without FePt NPs under the same conditions. The GISAXS data suggest that the addition of NPs accelerates the solvent evaporation, leading to a faster film formation of the hybrid film compared to the pure film. As the solvent is almost evaporated, a metastable state is observed in both films. Compared with the pure film, such a metastable state continues longer during the printing process of the hybrid film because of the presence of FePt NPs, which inhibits the reorganization of the DBC chains. Moreover, investigations of the field-dependent magnetization and temperature-dependent susceptibility indicate that the printed hybrid film is superparamagnetic, which makes this film class promising for magnetic sensors.

1. Introduction

Magnetic films have captured great research attention in applications of magnetic sensors, inductors, magnetic energy, and data storages.[1–4] For some special applications, flexible magnetic films are essential.[5–8] For example, in case of wearable magnetic sensors, their ability to withstand mechanical deformation depends of the flexibility of the magnetic films. Moreover, such deformation upon a magnetic force can result in an amplified current to be output in a suspended gate organic field effect transistor as a non-contact controller.[6] To achieve flexible magnetic films, polymers are regarded as well suited candidates to act as a soft matrix to host hard magnetic nanoparticles (NPs).[9] Polymers are flexible, lightweight, and easy to process with wet chemical methods and therefore have gained increasing attention in device fabrication.[7] In particular, diblock copolymers

W. Cao, S. Yin, S. Liang, M. A. Scheel, P. Müller-Buschbaum
Lehrstuhl für Funktionelle Materialien
Physik-Department
Technische Universität München
James-Franck-Straße 1, 85748 Garching, Germany
E-mail: muellerb@ph.tum.de

M. Bitsch, M. Gallei
Chair in Polymer Chemistry
Saarland University
Campus C4 2, 66123 Saarbrücken, Germany

M. Plank
Ernst-Berl-Institute for Technical and Macromolecular Chemistry
Technische Universität Darmstadt
Alarich-Weiss-Straße 4, 64287 Darmstadt, Germany

M. Opel
Walther-Meissner-Institut
Bayerische Akademie der Wissenschaften
Walther-Meissner-Straße 8, 85748 Garching, Germany

O. Janka
Inorganic Solid-State Chemistry
Saarland University
Campus C4 2, 66123 Saarbrücken, Germany

M. Schwartzkopf, S. V. Roth
Deutsches Elektronen-Synchrotron (DESY)
Notkestraße 85, 22607 Hamburg, Germany

S. V. Roth
Department of Fibre and Polymer Technology
KTH Royal Institute of Technology
Teknikringen 56-58, Stockholm SE-100 44, Sweden

P. Müller-Buschbaum
Heinz Maier-Leibnitz Zentrum (MLZ)
Technische Universität München
Lichtenbergstraße 1, 85748 Garching, Germany

(DBCs) have been proven as a powerful matrix and an effective template to host NPs, due to the ability to form various periodic nanostructures (such as cylinders, lamellae, and spheres).[10–12] Moreover, the DBC-assisted magnetic NPs assembly is also an effective approach to control the NP arrangement inside the polymer matrix due to the different interactions of the NPs with the two blocks of the DBC.

Various methods, such as spin coating, solution casting, spray coating, and printing, have been developed for the wet chemical fabrication of magnetic hybrid NP-DBC films.[13–15] For instance, Konefał et al. prepared magnetic hybrid films by spin coating, in which iron oxide (magnetite, Fe_3O_4) NPs were dispersed uniformly inside the P4VP domains of the DBC polystyrene-*block*-poly(4-vinylpyridine) (PS-*b*-P4VP).[13] Hammond et al. fabricated nanocomposite films containing a cylindrical polystyrene-*block*-poly(2-vinylpyridine) (PS-*b*-P2VP) DBC and spindle type hematite (α-Fe_2O_3) NPs via a solution casting method.[14] The alignment of the α-Fe_2O_3 NPs can be further improved by employing a uniaxial external magnetic field during solution casting. In our previous studies, various methods, like spin coating, spray coating, and printing, were utilized to prepare magnetic NP-DBC films with different morphologies and magnetic properties.[15–17] Among these fabrication methods, printing has obtained increasing attention because of its large-scale production capability in industrial applications.[15,18,19] Moreover, printing is an effective method to obtain homogeneous films with smooth surfaces on a macroscopic level compared to other methods such as spray coating. To achieve a favorable morphology, it is necessary to have a systematic investigation on the morphological evolution of hybrid NP-DBC films during printing process.

During the printing process, grazing-incidence small-angle X-ray scattering (GISAXS) has been proven to be an effective approach to track the morphology evolution without destroying the films.[18,20–22] For instance, Liu et al. employed in situ GISAXS measurements to study the morphology evolution in slot-die printed polymer-based active layers during the drying process.[18] Pröller et al. studied the morphology evolution of [6,6]-phenyl-C_{61}-butyric acid methyl ester aggregation in printed active layers via in situ GISAXS.[20] Zhu et al. reported the real-time evolution of PTzBI-Si:N2200 blend films during printing based on in situ GISAXS.[21] With in situ GISAXS, Marques et al. and Gu et al. followed the structure evolution during film drying process in PS-*b*-P2VP DBC and polyisoprene-*block*-polystyrene-*block*-poly(4-vinylpyridine) triblock terpolymer, respectively.[22,23] In our previous studies, the kinetics of printed different films, such as PbS quantum dot stacking and bulk heterojunction films, were in-depth investigated via in situ GISAXS.[24,25]

To date, concerning magnetic NP-DBC hybrid films, less attention has focused on the kinetics of printed magnetic hybrid films during the film formation process. The kinetics of the magnetic hybrid films and the arrangement of the magnetic NPs inside the DBC films during the printing process are rarely investigated. Most studies focused on the final printed magnetic NP-DBC hybrid films.[7,15] In our previous studies, the kinetics of magnetic hybrid films during spray coating were successfully investigated.[17,26] However, spray coating is a layer-by-layer deposition technology, which is different from printing.

In the present study, the slot-die printing technique is applied to fabricate magnetic hybrid films by using an ultrahigh molecular weight (UHMW) DBC PS-*b*-PMMA to host magnetic iron platinum (FePt) NPs with a radius of around 3.8 ± 0.4 nm. We select 3 wt% of FePt NPs to avoid a significant NP aggregate formation, which would not only perturb the DBC nanostructure templating of the NP arrangement, but also allow for a reasonable magnetic response of the printed magnetic hybrid films. With in situ GISAXS, the kinetics of the magnetic hybrid NP-DBC films and the arrangement of the magnetic NPs during solvent evaporation are investigated. The structure formation in different stages of the film formation is monitored. As a reference, a pure DBC PS-*b*-PMMA film without magnetic NPs is printed under the same conditions. The surface structures and magnetic properties of the printed films are probed by scanning electron microscopy (SEM) and superconducting quantum interference device (SQUID) magnetometry, respectively. The in situ GISAXS data suggest that the addition of FePt NPs accelerates the solvent evaporation, leading to a faster film formation of the hybrid film compared to the pure DBC film. A metastable state is observed in both films when the solvent is almost evaporated. With in situ GISAXS measurements, the influence of the FePt NPs on the duration of such a metastable state and the microphase separation structure of the DBC film during printing is investigated. The obtained magnetic data show that the printed magnetic hybrid NP-DBC film is superparamagnetic, which is beneficial to scale up the flexible magnetic film fabrication for magnetic sensors.[16,26] Moreover, the present work provides a profound insight for the future optimization of printed magnetic hybrid NP-DBC films, as well as other hybrid NP-DBC systems (such as zirconium oxide NP-DBC and gold NP-DBC).[10,11]

2. Results and Discussion

2.1. Surface Morphology of the Final Printed Films

SEM is applied to examine the surface morphology of the final printed pure and hybrid films. The SEM images of the printed pure PS-*b*-PMMA film at low and high magnifications are shown in **Figure 1**a,c, respectively. The bright matrix and dark domains correspond to PS and PMMA blocks, respectively.[27] According to our previous study of UHMW PS-*b*-PMMA with a PMMA volume fraction of 0.172, PMMA cylinders dispersed in the PS matrix are expected as microphase separation structure.[17] This microphase-separated structure is attributed to the use of UHMW DBC, which exhibits a very high segregation strength between PS and PMMA blocks, according to the block ratio.[28] In Figure 1a,c, indeed parallel and perpendicular PMMA cylinders are observed. The average half-length of the parallel PMMA cylinders and average radius of the PMMA cylinders are about 27 ± 5 and 59 ± 11 nm, respectively.

For the hybrid NP-DBC film, magnetic FePt NPs (brighter spots) are observed in addition. The NPs are positioned inside the PMMA domains as shown in Figure 1b,d. In the hybrid film, the FePt NPs have a higher selectivity to the PMMA domains versus the PS phase because the FePt NPs are functionalized with PMMA chains. Moreover, less parallel PMMA cylinders are
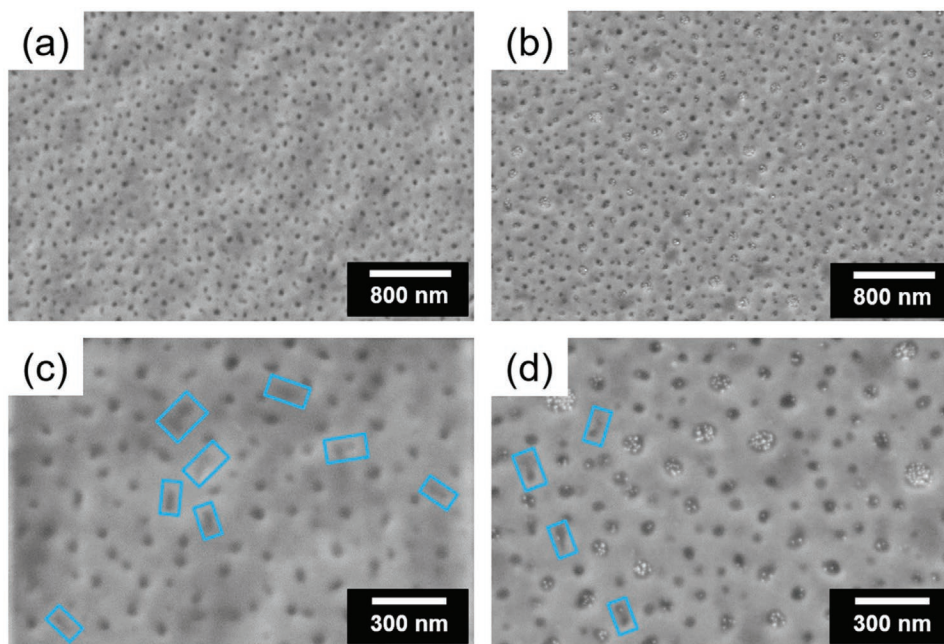
2107667 (2 of 9)

Figure 1. SEM images of printed films of a,c) pure PS-*b*-PMMA reference film and b,d) hybrid film containing 3 wt% of FePt NPs at low (a,b) and high (c,d) magnifications. The parallel PMMA cylinders are marked with blue rectangles in the high magnification images.

observed in the hybrid system (Figure 1d; Figure S5b, Supporting Information) compared with the pure film (Figure 1c; Figure S5a, Supporting Information). The parallel PMMA cylinders are marked with blue rectangles in Figure 1c,d and Figure S5, Supporting Information. Such decreased number of parallel cylinders can be attributed to the presence of a polymer-rich layer during the solvent evaporation and a strong interaction between the polymer and the functionalized FePt NPs.[29–31] It has been reported that a polymer-rich layer at the interface of liquid and vapor was formed during solvent evaporation of polymer solution.[31] The formed layer can attract more NPs to the interface if the interaction $F_{NP–polymer}$ is higher than the interaction $F_{NP–solvent}$. In case of the present study, the used FePt NPs are functionalized with PMMA chains and the DBC is PS-*b*-PMMA. Thus, the interaction $F_{NP–polymer}$ is strong enough to move some NPs to the interface, causing more PMMA chains (functionalized on NP surface) to appear on the sample surface. However, such behavior increases the contact area between air and PMMA, leading to an increase in the surface energy of the hybrid system due to a higher surface energy of PMMA ($\gamma_{PMMA} \approx 41$ mN m^{-1}) compared with that of PS ($\gamma_{PS} \approx 40$ mN m^{-1}).[32,33] To minimize the surface energy of the hybrid system, formation of more upstanding PMMA cylinders is supported. As a consequence, more PMMA domains are flipped from a parallel to a vertical orientation in the hybrid system.

2.2. Morphology Evolution during Printing

To study the impact of FePt NPs on the morphology evolution of PS-*b*-PMMA DBC film and the arrangement of the NPs during the film formation process, the film printing is combined with in situ GISAXS (as shown in Figure S6, Supporting Information). Printing is done at room temperature to see the structure evolution during solvent evaporation. This is different from our previous in situ studies on spray deposited magnetic NP-DBC films, which focused on the dry regime.[17,26] The sprayed films dried so fast that the morphological evolution during solvent evaporation process was not observed through in situ GISAXS. During printing, the DBC solution flows out along a solution guide mask and is then spread evenly on the substrate via movement of the sample holder.[24] For the in situ GISAXS measurements, we define the moment when the sample holder stops as $t = 0$ s.

For the pure PS-*b*-PMMA film (without FePt NPs), selected 2D GISAXS data at different times are displayed in Figure S7, Supporting Information. With increasing time, the overall signal intensity in the Yoneda peak region increases first due to the evaporation of solvent and then remains relatively stable in the later stages.[25] The DBC structure is developing along with the solvent evaporation. For the hybrid film containing 3 wt% FePt NPs, the selected 2D GISAXS data at different times are displayed in Figure S8, Supporting Information. Similar to the observations in the pure PS-*b*-PMMA film, the overall intensity in the Yoneda peak region increases first with increasing time, while it remains relatively stable at later stages.

To extract the DBC morphology changes during printing, horizontal line cuts of the 2D GISAXS data are performed (as indicated in Figure S7, Supporting Information with a red rectangle at $t = 0$ s). **Figure 2**a shows selected horizontal line cuts (black dots) of the printed pure PS-*b*-PMMA film at selected times from the in situ printing. All horizontal line cuts are displayed in an 2D intensity mapping for the pure PS-*b*-PMMA film in Figure 2b.[34] For the pure DBC film, it can be seen that the intensity along the q_y direction becomes relatively stable after $t = 18.9$ s (marked with a white dashed line), indicating
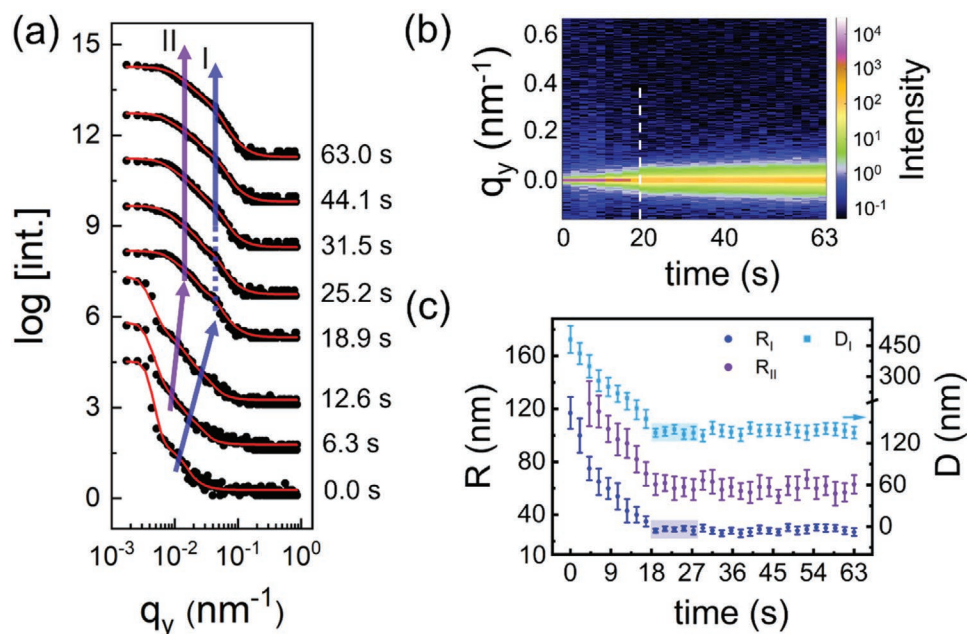
Figure 2. a) Selected horizontal line cuts of the 2D GISAXS data during printing of the pure PS-*b*-PMMA film at selected times (0.0, 6.3, 12.6, 18.9, 25.2, 31.5, 44.1, and 63.0 s from bottom to top). The fits are shown with red lines and shifted along the *y* axis together with their corresponding cuts. The structure factor contribution of PMMA domains and form factor contribution of PMMA elongated structure are denoted with I (blue arrow) and II (purple arrow), respectively. b) 2D mapping of all horizontal line cuts obtained from the 2D in situ GISAXS data during printing of the pure PS-*b*-PMMA film. c) Radii of the PMMA domains (R_I) and PMMA elongated structure (R_{II}) and distance of the PMMA domains (D_I) obtained from the fits. The semi-transparent colored area indicates a metastable state.

that the solvent is almost evaporated and a relatively stable film is formed.

For a quantitative insight, horizontal line cuts are modeled based on the effective interface approximation and the distorted wave Born approximation (DWBA).[35–37] Further information on the modeling can be seen in the Supporting Information. The corresponding fits and obtained radii of the pure PS-*b*-PMMA film are summarized in Figure 2a,c, respectively. Two main features (I and II) are observed (Figure 2a). Features I and II are structure factor contribution of the PMMA domains (perpendicular PMMA cylinders and parallel PMMA cylinders along the radial direction) and form factor contribution of the elongated PMMA structure (parallel PMMA cylinders along the length direction), respectively.

In the initial stage ($t \leq 18.9$ s), feature I shifts to higher q_y values with increasing time, indicating that the average center-to-center distance of the PMMA domains decreases over time. In more detail, the average radius and the average center-to-center distance of the PMMA domains decrease from 117 ± 12 to 28.1 ± 1.5 nm and 480 ± 67 to 135 ± 6 nm, respectively. Such decreases in the PMMA domain size and inter-domain distance are similar to the reported observations of the drying process of a block copolymer film.[23] The polymer chains shrink due to the solvent evaporation over time, leading to decreases in PMMA domain radius and inter-domain distance of neighboring PMMA domains. As the solvent is almost evaporated, the film changes from a wet state to a solid-like state and the mobility of polymer chains is strongly suppressed due to the lack of sufficient solvent molecules. Thus, feature I remains constant with further increasing time (after 18.9 s) with an average radius of

the PMMA domains of 28.1 nm and an average center-to-center distance of 135 nm. Looking in more detail, feature I turns out to be metastable in the time range from 18.9 to 27.3 s as seen from the increasing error bars marked with semi-transparent colors in Figure 2c, which indicates a loss in order. Such reorganization of the polymer chains is caused by a small amount of residual solvent inside the DBC film.[23] For $t > 27.3$ s, the error bars remain constant and since the average radius and the average center-to-center distance of the PMMA domains also remain constant within in the error bars, a final stable DBC film is obtained. In contrast, in our previous in situ studies on spray deposited magnetic NP-DBC films,[17,26] the DBC microphase structures remained almost stable during the entire spray process due to the lack of mobility of the polymer chains. Since an extremely rapid evaporation of the solvent happened in the spray process, the above-mentioned metastable state was not observed in our previous in situ studies.

Besides feature I, in the lower q_y region (0.010–0.015 nm⁻¹), an additional scattering feature (denoted as feature II, shown as a purple arrow in Figure 2a) is observed at $t \geq 6.3$ s. It arises from the form factor of elongated PMMA structures, which are ascribed to the parallel PMMA cylinders seen in the SEM images (Figure 1c). As time increases to 18.9 s, this feature II shifts to higher q_y values. The corresponding average radius of the elongated PMMA structure decreases from 124 ± 17 to 61 ± 8 nm. For $t \geq 18.9$ s, feature II remains constant as discussed for feature I. Error bars do not change for feature II. This may be because the reorganization of the polymer chains has a great influence on the radial size of the cylinders but has a small influence on the height or length of the cylinders.
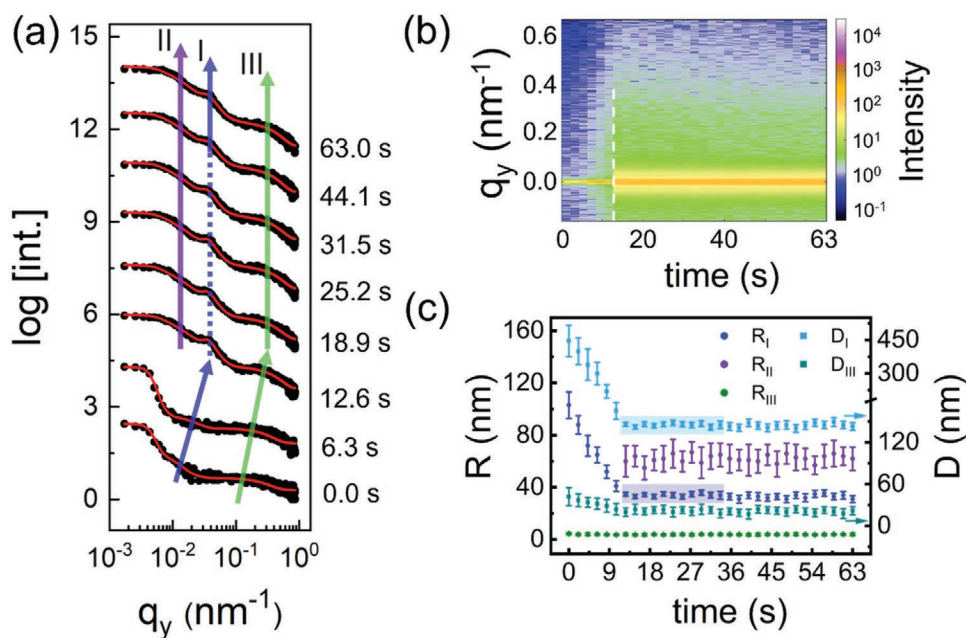
Figure 3. a) Selected horizontal line cuts of the 2D GISAXS data during printing of the hybrid film containing 3 wt% FePt NPs at selected times (0.0, 6.3, 12.6, 18.9, 25.2, 31.5, 44.1, and 63.0 s from bottom to top). The fits are shown with red lines and shifted along the y axis together with their corresponding cuts. The structure factor contributions of PMMA domains and FePt NPs are denoted with features I (blue arrow) and III (green arrow), respectively. The form factor contributions of PMMA elongated structure are denoted with II (purple arrow). b) 2D mapping of all horizontal line cuts obtained from the 2D GISAXS data during printing of the hybrid film. c) Radii of the PMMA domains (R_I), PMMA elongated structure (R_{II}), and FePt NPs (R_{III}) and distances of the PMMA domains (D_I) and of nearest neighbor FePt NPs (D_{III}) obtained from the fits. The semi-transparent colored areas indicate a metastable state.

Figure 3a shows selected horizontal line cuts from the 2D GISAXS data of the hybrid NP-DBC film and the corresponding fits. The 2D intensity mapping from all horizontal line cuts of hybrid NP-DBC film is shown in Figure 3b. Obviously, a relatively stable hybrid film is formed already at $t = 12.6$ s (Figure 3b), which is faster as compared to the pure PS-b-PMMA film ($t = 18.9$ s). This indicates that the addition of FePt NPs accelerates the majority of the solvent evaporation, which will be explained further below. For modeling of the horizontal line cuts, three characteristic features are required. Two features resemble the PMMA domains (perpendicular and parallel orientation) and the third feature the FePt NPs.

As shown in Figure 3a, in the hybrid film formation the evolution of feature I is similar to that of pure film. However, feature I of the hybrid film remains constant at $t \geq 12.6$ s, while in case of the reference film this happens at $t \geq 18.9$ s. Thus, the hybrid film dries faster compared to the pure film in terms of forming a metastable film during printing. Since the used solvent toluene exhibits a higher selectivity to PS versus PMMA, the solvent prefers to move to the surface to evaporate through the PS phase. The polymer-solvent interaction parameter is $\chi_{PS-toluene} = 0.34$ and $\chi_{PMMA-toluene} = 0.45$.[38] Less parallel PMMA cylinders are formed due to the presence of the NPs and more PS is at the surface of the hybrid film compared with the pure DBC film as observed from the SEM images. Thus, the solvent molecules have more chances to evaporate in the hybrid system. As the solvent evaporates faster, one might expect a less ordered DBC structure in the hybrid film versus the pure film, especially for the use of UHMW DBC.[39,40] In general, for long

polymer chains more time to phase separate into ordered structures is necessary.[39] However, instead of getting a less ordered DBC structure, feature I shows higher order at $t \geq 12.6$ s for the hybrid film containing 3 wt% FePt NPs (marked with blue arrow in Figure 3a) compared with the pure film (marked with blue arrow in Figure 2a). Such increased order of the DBC structure in the hybrid film originates from the reduced number of parallel PMMA cylinders (as seen in SEM) due to the addition of the FePt NPs. The more parallel PMMA cylinders are present, the more they disturb the DBC structure,[17] because they are distributed in the film with random orientations (Figure 1). With further increasing time, again an increase in the error bars of feature I is observed (from 12.6 to 33.6 s, marked with semi-transparent colors in Figure 3c). The respective metastable state of the hybrid film is longer (21.0 s) as compared to the pure DBC (8.4 s). Obviously, the presence of the FePt NPs limits the movement of the polymer chains, while residual solvent molecules enable a local reorganization of the polymer chains.[9] As shown in Figure 3c, the average center-to-center distance of the PMMA domains decreases in the beginning of the film formation and remains constant around 146 ± 5 nm (Figure 3c) at $t \geq 12.6$ s. Comparing the final printed films, the PMMA domains (feature I) are larger for the hybrid film (average radius 33.4 ± 2.7 nm, Figure 3c) compared with the pure DBC film (28.1 ± 2.5 nm, Figure 2c) due to the space required for accommodating the FePt NPs inside the PMMA domains.

Similar to the pure DBC film, a constant feature II (elongated PMMA structure) is seen at lower q_y values after
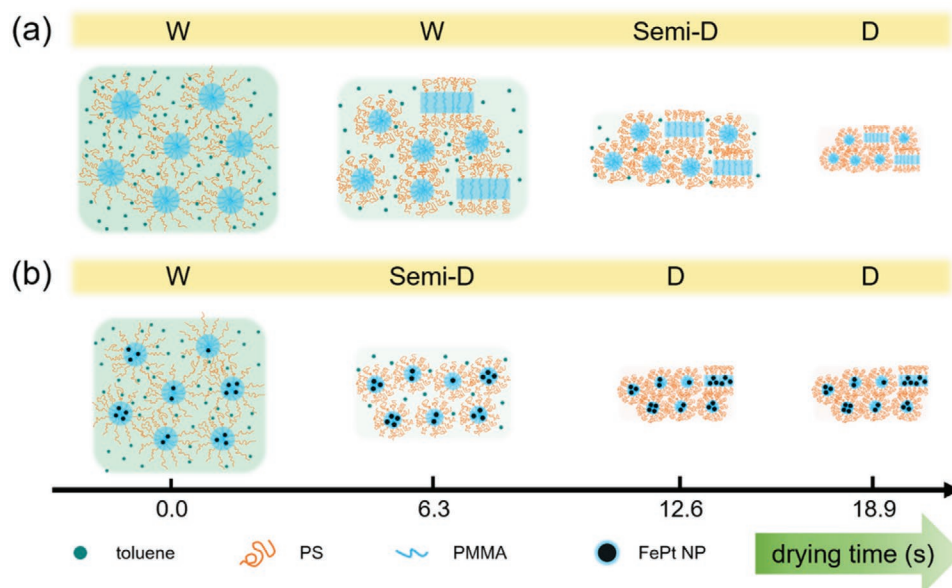
Figure 4. Top-view sketch of the main morphology evolution during printing for a) pure and b) hybrid films from a wet state (W) to a semi-dry state (Semi-D) to a dry state (D), in which the solvent is almost evaporated. The states are shown at different times as indicated in the bottom of the sketch. The green dots only represent the amount of solvent (toluene).

a relatively stable film has formed ($t \geq 12.6$ s). The corresponding average radius of the elongated PMMA structure remains constant at around 63 ± 8 nm (Figure 3b). However, we do not see a decrease of feature II at the early stages of the solvent evaporation, which is different to the observation in the pure DBC film. Such difference can be explained by the formation of fewer parallel PMMA cylinders in the hybrid film compared with the pure DBC film due to the addition of FePt NPs. As a result, these parallel PMMA cylinders are located sparsely inside the semi-dry film and do not have a sufficient scattering contribution to be seen in the GISAXS measurements. With further solvent evaporation, the number of parallel PMMA cylinders per unit volume gradually increases and finally passes the threshold to be detectable in the GISAXS data at $t \geq 12.6$ s.

At the studied NP concentration, the FePt NPs are no longer dispersed only as isolated NPs but also aggregate. Consequently, for the hybrid film, one more structure factor is required to model the inter-domain distance of neighboring FePt NPs, which is denoted as feature III (marked with a green arrow in Figure 3a). The form factor representing the radius of NPs remains constant during the entire film formation, since the size of the FePt NPs does not change during the printing.[41,42] Information about the PMMA chains located on the NP surface during printing is gained from analyzing the nearest neighbor distance of the NP. As seen in Figure 3a, the feature III shifts to higher q_y values with increasing until 12.6 s, which is similar to the changes of feature I. The corresponding average nearest neighbor distance of the FePt NPs decreases from 42 ± 13 to 20 ± 6 nm (Figure 3b), while the average FePt NP radius is 3.9 ± 0.6 nm (Figure 3c). When $t \geq 12.6$ s, feature III remains constant due to the absence of mobility of NPs caused by an almost complete evaporation of the solvent.

2.3. Visualization of the Main Morphology Evolution

During printing, the main morphology evolution occurs before the solvent almost evaporates. To better show the main morphology evolution, a top-view sketch of the film formation of the DBC without (**Figure 4**a) and with FePt (Figure 4b) NPs during the print process until the solvent almost evaporates is illustrated. Initially, a wet (W) film is deposited. During the drying process, both PS and PMMA chains shrink as the solvent evaporates, leading to a decrease in the size and the center-to-center distance of the PMMA domains. Due to the presence of SiO$_x$ on the Si substrate, which is preferentially wetted by the PMMA block, parallel PMMA cylinders should form. In case of the pure DBC printing, parallel PMMA cylinders are observed during the wet (W) stage in the GISAXS measurements.[43,44] Similar to the PMMA domains, the size of these parallel PMMA cylinders decrease over time. In contrast, in the hybrid film printing parallel PMMA cylinders are not observed during wet (W) and semi-dry (Semi-D) stages via GISAXS measurements. They appear at the last stage, namely the dry (D) stage as explained by the formation of less parallel PMMA cylinders in the hybrid film compared with the pure film as discussed before. Importantly, the hybrid film exhibits a faster drying speed than the pure DBC film due to the different selectivity of the solvent to PS and PMMA and the different proportions of PS and PMMA on the surface for pure and hybrid films. The final dry (D) films differ in their characteristic domain sizes due to the presence of the NPs in the hybrid film.

2.4. Magnetic Properties

For the analysis of the magnetic properties of final printed hybrid film, measurements are performed at different temperatures via
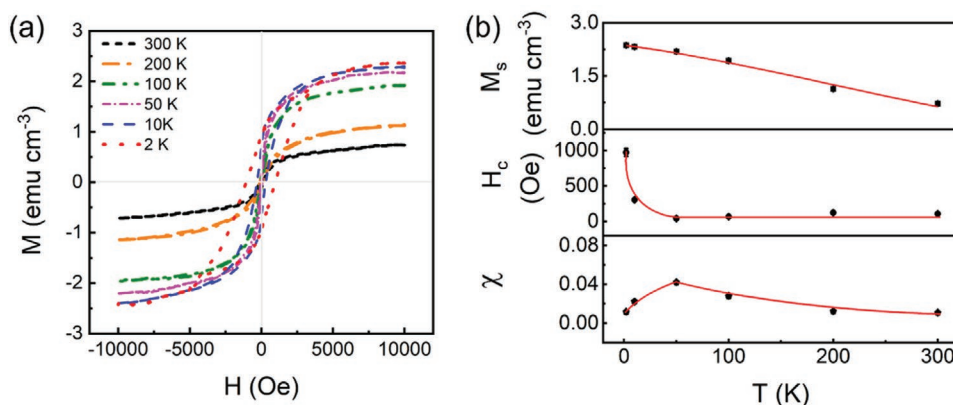
Figure 5. a) Magnetization curves of the printed hybrid film obtained at various temperatures plotted against magnetic field (from −10 000 to 10 000 Oe). b) Saturation magnetization (M_s), coercivity (H_c), and magnetic susceptibility (χ) versus temperature obtained from the magnetization curves. The solid red lines serve as guides to the eye.

a SQUID magnetometer. **Figure 5**a shows magnetization curves of the printed hybrid film for temperatures between 2 and 300 K. At 2 and 10 K, the magnetization curves exhibit a hysteresis loop. With increasing temperature, the hysteresis loop narrows and finally disappears at $T \geq 50$ K, indicating a superparamagnetic behavior of the printed hybrid film.[45,46] Such behavior differs from our previous study on ferromagnetic hybrid polymer films, which exhibited obvious hysteresis loops with large hysteresis for all temperatures.[17] To further quantify the relationship between magnetic properties and temperature, the corresponding saturation magnetization (M_s), coercivity (H_c) and magnetic susceptibility (χ) are shown in Figure 5b.

As the temperature increases, M_s decreases due to thermal fluctuations,[47,48] which leads to faster fluctuations in magnetic moments and higher random anisotropy in the magnetic domains with increasing temperature. As a result, lower M_s values are obtained at higher temperatures. Due to the superparamagnetic behavior of the used fcc-FePt NPs, H_c decreases sharply first and then remains constant with a value of almost zero.[49,50] At low temperatures (2 and 10 K), the thermal energy is too small to overcome the anisotropy energy and the magnetic moments are blocked along the applied external magnetic field.[1,7] As the temperature increases, such blocked behavior is weakened, resulting in a decrease of H_c. While at high temperatures ($T \geq 50$ K), the anisotropy energy can be overcome by the high thermal energy.[1] In this case, magnetic moments can spontaneously reverse themselves when the external magnetic field is removed, leading to an H_c of almost zero. Moreover, a non-monotonic temperature dependence of the χ is observed as shown in Figure 5b. With increasing the temperature from 2 to 50 K, χ increases from 0.0115 ± 0.0012 to 0.0421 ± 0.0007. This increase results from a faster fluctuation of the magnetic moments, yielding an enhanced magnetic response at a higher temperature.[26] However, when the magnetic moments can be spontaneously reversed, a further increase in temperature causes the magnetic moments to fluctuate quite fast and become more difficult to be aligned or controlled by an external magnetic field with a previous used strength.[51] Thus, χ decreases as the temperature increases from 50 to 300 K.

According to the changes in H_c and χ (Figure 5b), the characteristic blocking temperature (T_B) of the superparamagnetic hybrid film is expected to be between 10 and 50 K. To quantify T_B, field-cooling (FC) and zero-FC (ZFC) measurements are performed for the printed hybrid film at an applied external magnetic field of 100 Oe. **Figure 6** shows the obtained FC and ZFC curves in the range of 2 to 300 K. A peak is observed at a temperature of around 24 K (marked with an arrow), indicating the T_B of the printed hybrid film is 24 K. Such value is much smaller than the T_B (121 K) reported in our previous wet-chemically processed magnetic film study,[26] due to the unique properties of the used fcc-FePt NPs.[50,52] Thus, the hysteresis loops are observed at temperatures (2 and 10 K) below 24 K and disappear at temperatures above 24 K, such as 50, 100, 200, and 300 K (Figure 5a).

3. Conclusion

The influence of the presence of FePt NPs on the film formation of UHMW PS-*b*-PMMA DBC films is investigated by in
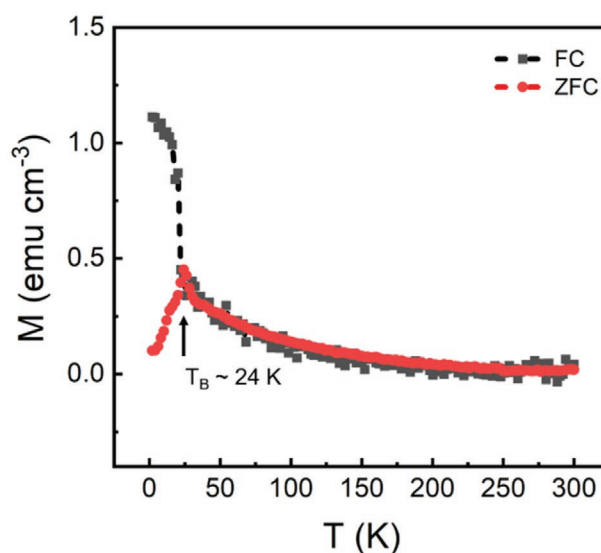

Figure 6. FC (black square) and ZFC (red sphere) curves for printed hybrid film obtained at a magnetic field of 100 Oe.

**ADVANCED
SCIENCE NEWS**
www.advancedsciencenews.com

**ADVANCED
FUNCTIONAL
MATERIALS**
www.afm-journal.de

situ experiments during printing. A printed pure DBC PS-*b*-PMMA film serves as a reference to understand the impact of the NPs. The structure formation is monitored with in situ GISAXS measurements. For both films, pure and hybrid, the size of PMMA domains decreases as the solvent evaporates from the initially deposited wet film. Compared to the pure film, the hybrid film exhibits a faster shrinkage of the PMMA domains due to the addition of NPs, which accelerates the solvent evaporation. As a result, a faster formation of a metastable state is observed in the hybrid film compared with the pure film. The metastable state changes slightly as the time increases due to the reorganization of polymer chains enabled by a small amount of residual solvent molecules inside the printed film. Since the presence of the FePt NPs hinders the reorganization of the polymer chains, a longer metastable state is observed during the printing of hybrid film compared with the pure film. In addition, less parallel oriented microphase-separated structures of the DBC are formed in the hybrid film compared to the pure film, which results in a higher ordered structure of the hybrid film when the solvent is almost evaporated. Similar to the PMMA domains, the size of the parallel DBC microphase separation structure is decreased as the solvent evaporates from the pure film. However, we do not see the similar shrinkage at the beginning of the solvent evaporation in case of the hybrid film because of the formation of less parallel PMMA cylinders in the hybrid film compared with the pure film. This leads to a weak scattering contribution, which is not detected in the GISAXS measurements of the hybrid film. Moreover, magnetic data reveal that the printed hybrid film is superparamagnetic, which is important for the fabrication of magnetic films used in magnetic sensors on a large scale. Overall, our study provides insights for the future optimization of printed magnetic NP-DBC hybrid films, as well as the hybrid systems based on DBC and other types of non-magnetic NPs.

4. Experimental Section

Printing Solutions Preparation: Two PS-*b*-PMMA solutions with and without FePt NPs were prepared in toluene with a fixed DBC concentration of 7 mg mL^{-1}. For the PS-*b*-PMMA solution with FePt NPs, an NP concentration (weight ratio between NPs and PS-*b*-PMMA) of 3 wt% was studied. Information on materials of PS-*b*-PMMA and FePt NPs are detailed in the Supporting Information.

Sample Preparation: Printing was performed on a pre-cleaned silicon substrate with a custom-made slot-die coater at room temperature.[53] To achieve a favorable film thickness, the solution flow rate, printing velocity, and distance between the mask and the substrate were set to 0.1 mL min^{-1}, 5 mm s^{-1}, and 0.5 mm, respectively.

Characterizations: GISAXS measurements were performed in situ at the P03 beamline (PETRA III, DESY, Germany) during the printing. The scattering signal was recorded on a 2D detector (LAMBDA 750k, X-Spectrum GmbH) with a pixel size of 55 µm × 55 µm with 20 cycles. Each cycle consisted of 0.1 s X-ray exposure time and 2.0 s waiting time. To track the morphology of films over a large area and to avoid beam damage, the in situ GISAXS measurements were carried out at different spots of the film through laterally moving the sample. The surface morphology of the final printed films was investigated with SEM measurements. The magnetic properties of the hybrid film were probed with SQUID magnetometry measurements. The detailed characterizations descriptions can be found in the Supporting Information.

Supporting Information

Supporting Information is available from the Wiley Online Library or from the author.

Conflict of Interest

The authors declare no conflict of interest.

Data Availability Statement

The data that support the findings of this study are available from the corresponding author upon reasonable request.

[1] L. Wu, A. Mendoza-Garcia, Q. Li, S. Sun, *Chem. Rev.* **2016**, *116*, 10473.

[2] I. Oh, J. Park, D. Choe, J. Jo, H. Jeong, M.-J. Jin, Y. Jo, J. Suh, B.-C. Min, J.-W. Yoo, *Nat. Commun.* **2021**, *12*, 1057.

[3] J. Huang, H. Wang, Z. Qi, P. Lu, D. Zhang, B. Zhang, Z. He, H. Wang, *Nano Lett.* **2021**, *21*, 1032.

[4] J. M. Galloway, J. E. Talbot, K. Critchley, J. J. Miles, J. P. Bramble, *Adv. Funct. Mater.* **2015**, *25*, 4590.

[5] M. Melzer, J. I. Mönch, D. Makarov, Y. Zabila, G. S. Cañón Bermúdez, D. Karnaushenko, S. Baunack, F. Bahr, C. Yan, M. Kaltenbrunner, O. G. Schmidt, *Adv. Mater.* **2015**, *27*, 1274.

[6] Y. Zang, F. Zhang, D. Huang, C. Di, D. Zhu, *Adv. Mater.* **2015**, *27*, 7979.

[7] S. Xia, L. Song, V. Körstgens, M. Opel, M. Schwartzkopf, S. V. Roth, P. Müller-Buschbaum, *Nanoscale* **2018**, *10*, 11930.

[8] R. Guo, X. Sun, B. Yuan, H. Wang, J. Liu, *Adv. Sci.* **2019**, *6*, 1901478.

[9] B. Sarkar, P. Alexandridis, *Prog. Polym. Sci.* **2015**, *40*, 33.

[10] D.-P. Song, C. Li, W. Li, J. J. Watkins, *ACS Nano* **2016**, *10*, 1216.

[11] N. Yan, X. Liu, J. Zhu, Y. Zhu, W. Jiang, *ACS Nano* **2019**, *13*, 6638.

[12] S. Kang, D. Y. Ryu, E. Ringe, R. J. Hickey, S.-J. Park, *ACS Nano* **2020**, *14*, 12203.

[13] M. Konefał, P. Černoch, V. Patsula, E. Pavlova, J. Dybal, K. Załęski, A. Zhigunov, *ACS Appl. Mater. Interfaces* **2021**, *13*, 9195.

[14] M. R. Hammond, H. Dietsch, O. Pravaz, P. Schurtenberger, *Macromolecules* **2010**, *43*, 8340.

[15] S. Xia, L. Song, W. Chen, V. Körstgens, M. Opel, M. Schwartzkopf, S. V. Roth, P. Müller-Buschbaum, *ACS Appl. Mater. Interfaces* **2019**, *11*, 21935.

[16] Y. Yao, E. Metwalli, M. Opel, M. Haese, J.-F. Moulin, K. Rodewald, B. Rieger, P. Müller-Buschbaum, *Adv. Mater. Interfaces* **2016**, *3*, 1500712.

[17] W. Cao, S. Yin, M. Plank, A. Chumakov, M. Opel, W. Chen, L. P. Kreuzer, J. E. Heger, M. Gallei, C. J. Brett, M. Schwartzkopf, A. A. Eliseev, E. O. Anokhin, L. A. Trusov, S. V. Roth, P. Müller-Buschbaum, *ACS Appl. Mater. Interfaces* **2021**, *13*, 1592.

[18] F. Liu, S. Ferdous, E. Schaible, A. Hexemer, M. Church, X. Ding, C. Wang, T. P. Russell, *Adv. Mater.* **2015**, *27*, 886.

[19] S. Chung, K. Cho, T. Lee, *Adv. Sci.* **2019**, *6*, 1801445.

[20] S. Pröller, F. Liu, C. Zhu, C. Wang, T. P. Russell, A. Hexemer, P. Müller-Buschbaum, E. M. Herzig, *Adv. Energy Mater.* **2016**, *6*, 1501580.

[21] L. Zhu, W. Zhong, C. Qiu, B. Lyu, Z. Zhou, M. Zhang, J. Song, J. Xu, J. Wang, J. Ali, W. Feng, Z. Shi, X. Gu, L. Ying, Y. Zhang, F. Liu, *Adv. Mater.* **2019**, *31*, 1902899.

[22] D. S. Marques, R. M. Dorin, U. Wiesner, D.-M. Smilgies, A. R. Behzad, U. Vainio, K.-V. Peinemann, S. P. Nunes, *Polymer* **2014**, *55*, 1327.

[23] Y. Gu, R. M. Dorin, K. W. Tan, D.-M. Smilgies, U. Wiesner, *Macromolecules* **2016**, *49*, 4195.

[24] W. Chen, H. Tang, N. Li, M. A. Scheel, Y. Xie, D. Li, V. Körstgens, M. Schwartzkopf, S. V. Roth, K. Wang, X. W. Sun, P. Müller-Buschbaum, *Nanoscale Horiz.* **2020**, *5*, 880.

[25] D. Yang, S. Grott, X. Jiang, K. S. Wienhold, M. Schwartzkopf, S. V. Roth, P. Müller-Buschbaum, *Small Methods* **2020**, *4*, 2000418.

[26] S. Xia, L. Song, N. Hohn, K. Wang, S. Grott, M. Opel, M. Schwartzkopf, S. V. Roth, P. Müller-Buschbaum, *Adv. Funct. Mater.* **2019**, *29*, 1808427.

[27] S. Ouk Kim, H. H. Solak, M. P. Stoykovich, N. J. Ferrier, J. J. de Pablo, P. F. Nealey, *Nature* **2003**, *424*, 411.

[28] V. Pryamitsyn, V. Ganesan, *Macromolecules* **2006**, *39*, 8499.

[29] K. E. Strawhecker, S. K. Kumar, J. F. Douglas, A. Karim, *Macromolecules* **2001**, *34*, 4669.

[30] L. Wang, Z. Zhang, Y. Ding, *Soft Matter* **2013**, *9*, 4455.

[31] S. Cheng, G. S. Grest, *ACS Macro Lett.* **2016**, *5*, 694.

[32] Y. Lin, C. Abetz, X. Li, J. Wang, T. Emrick, S. Long, Q. Wang, A. Balazs, T. P. Russell, *Nature* **2005**, *434*, 55.

[33] Y. Luo, D. Montarnal, S. Kim, W. Shi, K. P. Barteau, C. W. Pester, P. D. Hustad, M. D. Christianson, G. H. Fredrickson, E. J. Kramer, C. J. Hawker, *Macromolecules* **2015**, *48*, 3422.

[34] R. Lazzari, *J. Appl. Crystallogr.* **2002**, *35*, 406.

[35] Y. Yoneda, *Phys. Rev.* **1963**, *131*, 2010.

[36] P. Müller-Buschbaum, *Anal. Bioanal. Chem.* **2003**, *376*, 3.

[37] G. Renaud, R. Lazzari, F. Leroy, *Surf. Sci. Rep.* **2009**, *64*, 255.

[38] H. Jung, S. Woo, Y. Choe, D. Y. Ryu, J. Huh, J. Bang, *ACS Macro Lett.* **2015**, *4*, 656.

[39] J. K. D. Mapas, T. Thomay, A. N. Cartwright, J. Ilavsky, J. Rzayev, *Macromolecules* **2016**, *49*, 3733.

[40] M. Appold, M. Gallei, *ACS Appl. Polym. Mater.* **2019**, *1*, 239.

[41] T. Thurn-Albrecht, J. Schotter, G. A. Kastle, N. Emley, T. Shibauchi, L. Krusin-Elbaum, K. Guarini, C. T. Black, M. T. Tuominen, T. P. Russell, *Science* **2000**, *290*, 2126.

[42] I. Barandiaran, G. Kortaberria, *RSC Adv.* **2015**, *5*, 95840.

[43] S. Wu, *J. Phys. Chem.* **1970**, *74*, 632.

[44] K. Brassat, D. Kool, C. G. A. Nallet, J. K. N. Lindner, *Adv. Mater. Interfaces* **2020**, *7*, 1901605.

[45] X. Jiang, J. Feng, L. Huang, Y. Wu, B. Su, W. Yang, L. Mai, L. Jiang, *Adv. Mater.* **2016**, *28*, 6952.

[46] H. Wu, M. Khdour, P. Apsangi, H. Yu, *IEEE Trans. Magn.* **2017**, *53*, 1.

[47] W. F. Brown, *Phys. Rev.* **1963**, *130*, 1677.

[48] M. Pauly, B. P. Pichon, P. Panissod, S. Fleutot, P. Rodriguez, M. Drillon, S. Begin-Colin, *J. Mater. Chem.* **2012**, *22*, 6343.

[49] S. Maenosono, T. Suzuki, S. Saita, *J. Magn. Magn. Mater.* **2008**, *320*, L79.

[50] P. de la Presa, T. Rueda, A. Hernando, J. M. Ramallo-López, L. J. Giovanetti, F. G. Requejo, *J. Appl. Phys.* **2008**, *103*, 103909.

[51] K. Wiemer, K. Dörmbach, I. Slabu, G. Agrawal, F. Schrader, T. Caumanns, S. D. M. Bourone, J. Mayer, J. Steitz, U. Simon, A. Pich, *J. Mater. Chem. B* **2017**, *5*, 1284.

[52] N. T. T. Trang, T. T. Thuy, K. Higashimine, D. M. Mott, S. Maenosono, *Plasmonics* **2013**, *8*, 1177.

[53] K. S. Wienhold, C. L. Weindl, S. Yin, T. Tian, M. Schwartzkopf, A. Rothkirch, S. V. Roth, P. Müller-Buschbaum, *ACS Appl. Mater. Interfaces* **2020**, *12*, 40381.

2107667 (9 of 9)